Published in final edited form as:
J Biomech Eng. 2008 April ; 130(2): 021013.

Measurement of the Dynamic Shear Modulus of Mouse Brain Tissue *In Vivo* By Magnetic Resonance Elastography

Stefan M. Atay[1], **Christopher D. Kroenke**[3], **Arash Sabet**[1], and **Philip V. Bayly**[1,2]

1*Department of Mechanical and Aerospace Engineering Washington University*

2*Department of Biomedical Engineering Washington University*

3*Advanced Imaging Research Center Oregon Health and Science University*

Abstract

In this study, the magnetic resonance elastography (MRE) technique was used to estimate the dynamic shear modulus of mouse brain tissue *in vivo*. The technique allows visualization and measurement of mechanical shear waves excited by lateral vibration of the skull. Quantitative measurements of displacement in three dimensions (3-D) during vibration at 1200 Hz were obtained by applying oscillatory magnetic field gradients at the same frequency during an MR imaging sequence. Contrast in the resulting phase images of the mouse brain is proportional to displacement. To obtain estimates of shear modulus, measured displacement fields were fitted to the shear wave equation. Validation of the procedure was performed on gel characterized by independent rheometry tests and on data from finite element simulations. Brain tissue is, in reality, viscoelastic and nonlinear. The current estimates of dynamic shear modulus are strictly relevant only to small oscillations at a specific frequency, but these estimates may be obtained at high frequencies (and thus high deformation rates), non-invasively throughout the brain. These data complement measurements of nonlinear viscoelastic properties obtained by others at slower rates, either *ex vivo* or invasively.

Keywords

Elastography; MRI; brain; stiffness

INTRODUCTION

Characterization of tissue material properties is important in a number of ways to medical clinicians and researchers. Changes in material stiffness can indicate the presence of tumors and other diseases [1]. In the case of deep venous thrombosis (DVT), hardness of the thrombus is closely related to thrombus maturity, which in turn determines the appropriate course of treatment [2]. Physicians have long relied on hand palpation to detect the presence of a tumor where other imaging methods such as ultrasound, CT, and MRI have failed to do so. Techavipoo [3] notes that elastography (imaging of tissue stiffness) can be used to monitor a patient's response to cancer treatment.

Knowledge of brain material properties is also relevant to understanding the mechanisms of concussion and other types of traumatic brain injury (TBI). The mechanical properties of brain tissue govern how it deforms during an impact or high acceleration. The strain imposed on the brain during TBI has been of interest to researchers for more than sixty years, and methods for

Address for correspondence: Philip V. Bayly Mechanical and Aerospace Engineering Washington University 1 Brookings Drive, Box 1185 St. Louis, MO 63130 TEL: 314−935−6081 FAX: 314−935−4014 Email: pvb@me.wustl.edu.

accurately measuring the strain field in the brain during acceleration continue to be developed [4,5]. Margulies [6] developed an empirical correlation between critical shear strain and the onset of diffuse axonal injury (DAI) in response to rotational inertial loading of the brain. Prange and Margulies [7] studied inhomogeneity and nonlinear viscoelastic behavior of brain tissue by *ex vivo* shear and compression tests. Gefen and Margulies [8] estimated viscoelastic material properties in live and dead (in situ) brain tissue by indentation of cortical surface exposed by craniotomy. Darvish and Crandall [9] used a viscoelastic model to characterize the nonlinear response of the bovine brain at frequencies as high as 200 Hz. These prior studies have illuminated the response of brain tissue primarily under large deformations, but the dynamic response of brain tissue at high frequencies (and thus high deformation rates) typical of impacts remains uncertain, as do the properties of interior structures of the intact, living brain.

Characterization of mechanical properties of the developing brain is also important for understanding the nature of brain development. In a proposed theory of cortical folding Van Essen [10] postulates that tension in axonal fibers pulls the cerebral cortex together to create outward folds. It remains unclear whether the levels of tension generated in axons are sufficiently large to deform brain tissue, but this question can be addressed by better knowledge of both axonal tension and tissue stiffness. Othman and co-authors [11] also note the importance of soft-tissue material characterization in understanding the physical mechanisms that regulate cell and tissue growth.

Magnetic resonance elastography (MRE) enables the visualization and measurement of mechanical waves propagating in 3-D throughout a sample. From this information the shear stiffness of the sample can be inferred [12,13,14]. Manduca and co-workers [14] characterized strain waves of 100−150 Hz *in vivo* in breast, brain, and muscle tissue and identified the presence of breast tumors using MRE. Othman and colleagues [11] used MRE at frequencies up to 585 Hz to measure the shear stiffness of frog oocyte nucleui on a microscopic scale. Shear modulus estimates of a human brain using MRE have been reported by McCracken and colleagues [15]. Romano and co-workers [16] proposed a method to use MRE to study anisotropic materials, particularly transversely isotropic, leading to constrained propagation of elastic waves along the fiber directions in celery. Sinkus et al. [17] measured anisotropic and viscoelastic material properties in breast tissue and tumors by fitting MRE data to a corresponding model. Using ultrasound waves to induce motion in an agar gel, Plewes et al. [18] have shown that the technique is effective at frequencies as high as 515 kHz, and were able to detect displacement on the order of tens of nanometers. Lopez and co-workers [19] used MRE to characterize bovine articular cartilage at frequencies in excess of 1000 Hz.

In the current study we apply MRE to estimate the dynamic shear modulus of the mouse brain *in vivo*. The frequency used (1200 Hz) is well above those reported previously for *in vivo* experiments. Estimates of dynamic shear modulus, although subject to limitations inherent to MRE of the small animal brain, are expected to be valuable and complementary to material characteristics obtained by other approaches.

THEORY

MRE Principles

In MRE, oscillating shear displacements caused by harmonic vibration are measured from phase images obtained by modulating the gradient field of the MR scanner at the vibration frequency [12]. A schematic diagram of the MR pulse sequence is shown in Fig. 1. Application of this sequence leads to images in which phase contrast is developed between vibrating spins, as illustrated in Fig. 2.

If oscillating gradients of constant amplitude, frequency, and duration are applied in three orthogonal directions, a vector of motion-induced phase, $\vec{\varphi}$, is obtained at each voxel in the image space. The component of oscillatory displacement, $\vec{u}$, of the voxel is proportional to the phase, $\vec{\varphi}$, of the tissue spins obtained from elastography images [12]. Following Muthupillai et al. [12] we see that if the position of a spin packet in a 3-D sample is $\vec{r} = \vec{r}_o + \vec{u}$, and $\vec{u} = \vec{u}_o \cos\left(\omega t - \vec{k} \cdot \vec{r}_o + \theta\right)$ where $\vec{u}_o$, $\vec{r}_o$, ω, $\vec{k}_o$, and θ are the vibration amplitude, initial position of the spin packet, vibration frequency, spatial frequency vector, and vibration phase respectively, then the component of the phase vector in the direction of the gradient is:

$$\varphi_G\left(\vec{r}_o, \theta\right) = \gamma \int_0^{2\pi N/\omega} \left(\vec{G} \cdot \vec{r}\right) dt = \frac{\gamma \pi N \left(\vec{G}_o \cdot \vec{u}_o\right)}{\omega} \cos\left(\theta - \vec{k} \cdot \vec{r}_o\right) \tag{1}$$

[12], where $\phi_G(\vec{r}_o, \theta)$ is the component of the MR phase vector in the direction of $\vec{G}$; γ is the gyro-magnetic ratio of water, N is the number of cycles, $\vec{G} = \vec{G}_o \cos(\omega t)$ is the magnetic field gradient. The expression for displacement can be simplified to $\vec{u}\left(\vec{r}_o, \theta\right) = C\,\vec{\varphi}\left(\vec{r}_o, \theta\right)$, where C is a coefficient of proportionality. Since the gradients are applied in one direction at a time the coefficient of proportionality in the i^{th} direction is

$$C_i = \frac{u_{\max,i}}{\varphi_{\max,i}} = \frac{\omega}{\gamma \pi N G_{o,i}}, \tag{2}$$

where $G_{o,i}$ is the gradient amplitude in the i^{th} direction.

Shear Waves in Elastic Materials

In the current study, we use a linear, isotropic, elastic model to interpret the propagation of waves in mouse brain tissue. Although brain is a nonlinear, anisotropic, viscoelastic material, wave propagation involves small displacements at a specific frequency. Under specific conditions of small amplitude and a fixed frequency, a dynamic shear modulus may be used to describe tissue behavior. Also, although brain tissue is anisotropic in general, the magnitude of anisotropy measured *ex vivo* is not great [7]. Under suitable experimental conditions, anisotropic properties can be obtained by MRE. However, because of the challenges inherent to the small scale of the mouse brain, we performed this study using the simplest (isotropic) model to obtain average material properties, with the intention of pursuing studies of anisotropy in larger animals.

For a homogenous, isotropic, linearly elastic material undergoing small strain, the equation governing wave propagation in 3-D is:

$$\rho \frac{\partial^2 \vec{u}}{\partial t^2} = \mu \nabla^2 \vec{u} + (\lambda + \mu) \nabla\left(\nabla \cdot \vec{u}\right). \tag{3}$$

[20], where $\vec{u}$ is the displacement vector, μ is the shear modulus, ρ is the material density, and λ is a Lamé constant. In general, the displacement can be decomposed into transverse, longitudinal, and 'Hodge' components: $\vec{u} = \vec{u}_T + \vec{u}_L + \vec{u}_H$, where $\nabla \cdot \vec{u}_T = 0$, $\nabla \times \vec{u}_L = 0$, and $\nabla \times \vec{u}_H = \nabla \cdot \vec{u}_H = 0$ [16,17]. The transverse, or shear, displacement component $\vec{u}_T$ describes volume-conserving deformation. The transverse displacement is governed by

$$\rho \frac{\partial^2 \vec{u}_T}{\partial t^2} = \mu \nabla^2 \vec{u}_T. \tag{4}$$

If the motion is harmonic with excitation frequency ω

$$\frac{\partial^2 \vec{u}_T}{\partial t^2} = -\omega^2 \vec{u}_T. \tag{5}$$

Equation (4) can then be solved for μ, yielding

$$\mu = \frac{-\rho\omega^2 u_{T,i}}{\nabla^2 u_{T,i}}, i = x, y, z. \tag{6}$$

We note in passing that estimates of shear modulus can be made directly from phase measurements, without conversion to units of displacement. Since the displacement is simply proportional to phase, $\vec{u} = C\,\vec{\varphi}$, the previous equation can be written as

$$\mu = \frac{-\rho\omega^2 \varphi_{T,i}}{\nabla^2 \varphi_{T,i}}. \tag{7}$$

For a propagating sinusoidal shear wave, $\vec{u}_T = \tilde{\vec{u}}_T \quad \exp\left(i\left(\omega t - \vec{k}\cdot\vec{r}\right)\right)$, the Laplacian, $\nabla^2 u_{T,i} = -k^2 u_{T,i}$, where k is the magnitude of the spatial frequency vector, $\vec{k}$. Thus Eq. (6) can be written, for a propagating harmonic shear wave, as

$$\mu = \frac{\rho\omega^2}{k^2}. \tag{8}$$

METHODS

Animal Model

Adult female C57BL6 mice, 12−15 weeks old, weighing approximately 30 g were used in this study. Each mouse was anesthetized with 5% isoflurane in air and placed in an MR-compatible holder. A midline incision was made in the scalp to expose the cranium. A small plastic nut was glued (cyanoacrylate) to the skull to receive the tip of the actuation device (Fig. 3). Anesthesia was maintained at 1.5−2.0 % isoflurane in air for the duration of the experiment. Body temperature was maintained at 37°C by circulating warm water under the animal.

The mouse was placed in a stereotaxic holding apparatus which incorporated plastic ear bars and an incisor bar integrated into the anesthesia nose-cone. The ear bars minimized rigid-body motion of the skull, so that the motion detected by the MRE pulse sequence would be dominated by shear wave deformation of the brain, and not side-to-side translation or rotation of the entire head. The experimental setup allowed micro-meter scale vibrations to be transmitted from the actuator tip through the skull and into the brain. The holder and mouse were placed in a semi-cylindrical plastic tray for insertion into the MR scanner; vibration and MR imaging equipment and procedures are described in the following sections.

Data were obtained from six live animals. Data were also obtained from two animals that died during anesthesia and immobilization procedures, and were imaged *post mortem* within two hours of death. Procedures were reviewed by the Washington University Animal Studies Committee and performed in accordance with the Animal Welfare Act and the NIH Guide for the Care and Use of Laboratory Animals.

Wave generation

The electromagnetic actuator consisted of a coil of copper wire mounted on a plastic flexure with the coil axis horizontal and perpendicular to the magnetic field (Fig. 3). The assembly was mounted in the MR tray behind the animal. To maximize transmission of mechanical waves into the mouse brain the actuator arm was mechanically attached to the animal's skull. The free

end of the actuator arm had a small plastic screw tip protruding downward (Fig. 3). After the mouse was anesthetized and secured in the stereotaxic holder, the tip of the actuator was placed in the nut; the components were sized so that the threads of the screw and nut did not engage. To prevent the tip of the actuator from dislodging from the nut, an elastic band was stretched over the top of the actuator arm and secured around the ear bars on each end. A sinusoidal current was sent to the actuator to induce continuous (steady-state) lateral vibrations (~1−100 μm) of the tip.

Imaging

Imaging was performed on an 11.7T Varian (Palo Alto, CA) INOVA imaging system with high-performance gradient systems (Magnex, Oxford, UK). A spin-echo multi-slice MRI pulse sequence (Fig. 1) was modified with motion-sensitizing gradients, as described above under *Theory*. The motion-sensitizing gradients cause the nuclear spins to accumulate phase as they oscillate with the gradients. As a result the phase image of the data exhibits contrast proportional to displacement. To maintain symmetry in the spin-echo sequence, half the motion-sensitizing gradients were inserted on each side of the 180° pulse; the two trains of motion sensitizing gradient were separated by an integer number of motion cycles. Typical acquisition parameters were: repetition time t_r = 1 s; echo time t_e = 34 ms; 2 transients per line of k-space; 64 × 64 data matrix; field of view 16 mm × 16 mm; 15 slices; 0.1 mm gap between slices; slice thickness = 0.4 mm (voxels 0.25 × 0.25 × 0.4 mm). Data were interpolated to 0.125 × 0.125 × 0.25 mm for analysis and presentation.

To create waves with short wavelengths relative to the brain dimensions, vibrations were excited at 1200 Hz. Twelve cycles of the motion sensitizing gradients were completed on each side of the 180° pulse; the duration of this gradient oscillation was 10 ms. In validation experiments conducted at other frequencies, the 10 ms duration was held constant and the number of cycles varied in proportion to the excitation frequency (i.e., at 800 Hz, 8 cycles were used; at 400 Hz, 4 cycles). This not only kept the echo time and the duration of the pulse sequence constant, but since phase contrast increases with number of cycles, it compensates for the usual loss of amplitude at higher frequencies. The magnitude of the motion-sensitizing gradient was fixed at 10 Gauss/cm.

The sequence was run three times with the motion-sensitizing gradients applied in one of the three different directions: readout (inferior-superior); phase-encode (lateral); and slice-select (anterior-posterior). For each direction of motion measurement, images were acquired at 8 different temporal points in the excitation cycle by delaying image acquisition by a fraction (1/8, 2/8, 3/8, etc.) of the vibration period. Each set of eight images took approximately 15 minutes to acquire. An additional “baseline” image (see *Data Analysis* below) acquired with no vibration, took an additional 2 minutes to acquire. Thus to obtain data in all three directions, approximately one hour of imaging time was required.

Data Analysis

Because MRE relies on the phase of the MR image data, instead of its magnitude, it is necessary to subtract baseline phase errors so that all phase contrast is due to the periodic motion of the tissue and not due to field inhomogeneity or sampling errors. Thus two sets of data were collected for each direction of motion sensitization. In the first data set (“baseline”) the sample was imaged using the MRE pulse sequence, but with the actuator turned *off*. The second data set (“vibration”) was collected using the elastography pulse sequence, but with the actuator turned *on*, exciting mechanical waves in the tissue. By subtracting the phase of the “baseline” phase image from the phase of the “vibration” image, a data set where all of the phase contrast is due to wave motion in the tissue is obtained. The phase of the resulting image is directly

proportional to the displacement of the sample in the direction of the applied motion-sensitizing gradient.

Phase wrapping (due to 2π ambiguity in the phase of complex data) is an artifact common to all phase images. Commercial phase unwrapping software (Phase Vision™, Loughborough, UK) was used to unwrap the images.

The components of displacement at the excitation frequency were extracted by Fourier transforming the data with respect to time (i.e., over the 8 samples per excitation period), and retaining the Fourier coefficients corresponding to the excitation frequency [17].

The shear modulus governs propagation of transverse, or shear, waves (see Eq. (4)). Following Romano et al. [16], a Helmholtz decomposition of the displacement data was used to isolate the transverse component. The Helmholtz-Hodge decomposition was performed in the frequency domain [16]. Frequency domain decomposition introduces some artifacts due to truncation [21]. However, displacement amplitudes are naturally reduced near boundaries, providing a physical “windowing” effect that reduces truncation error. Data after Helmholtz-Hodge decomposition were compared to un-transformed data and were similar in amplitude and direction (i.e., deformation was dominated by shear). The divergence of the original displacement field was small, and was further reduced by Helmholtz decomposition, except for artifacts at edges. (Points within 2−4 voxels of edges are later eliminated from analysis since edge artifacts arise also in estimation of the Laplacian and fitting of the wave equation).

Two methods were used to estimate Laplacians of the displacement fields, since validation was done over a wide range of frequencies and wavelengths: (1) A standard central-difference scheme in the space domain, and (2) application of a second-derivative filter in the frequency domain. For data with long wavelengths relative to voxel size (high spatial resolution, > 16 voxels/wavelength), the Laplacian was obtained by applying standard central difference algorithm (the “gradient” function of Matlab™) in the space domain. For data characterized by short wavelength relative to voxel size (lower spatial resolution, < 16 voxels/wavelength), the Laplacian was estimated by filtering in the frequency domain v with a filter $f\left(\vec{k}\right) = -k^2 f_L(k)$. The factor of $-k^2$ in the frequency domain corresponds to the Laplacian operation in the space domain (as in Eq. (8)), and $f_L\left(\vec{k}\right)$ is a low-pass function (to reduce amplification of high-frequency noise), defined by

$$f_L(k) = \begin{cases} 1, k < k_0 \\ \exp\left(-\sigma\left(\frac{(k-k_0)^2}{k_0^2}\right)\right) \quad , k > k_0. \end{cases} \tag{9}$$

The low-pass cut-off frequency was set as $k_0 \approx 1.2$ the maximum spatial frequency in the shear waves. A 3×3 median filter was applied to the Laplacian estimate, in both cases. We have also obtained estimates of the Laplacian by computing analytical derivatives of fitted polynomial functions; this method provided very similar quantitative results to both methods, but took longer. Because all methods to estimate the Laplacian produce artifacts at the edge of the images, we eliminate edge voxels (2−4 voxels from the edge, depending on wavelength) from the fitting procedures below. In the mouse many of these edge voxels are in the scalp and muscle; in general, edge voxels exhibit relatively low displacement amplitude.

Estimates of shear modulus were obtained by locally fitting the wave equation (Eq. (6)) to data from the neighborhood of each voxel in the brain. Values of the transverse displacement and its Laplacian for all voxels within 1/6−1/4 wavelength from the reference point in the readout and phase-encode directions, and 1/12 −1/6 wavelength from the reference point in the slice direction at all phases in the vibration cycle, were simultaneously fitted to Eq. (6). The value

of shear modulus that minimized the squared error in the fit was taken as the estimate for that point (the density of brain was assumed to be the same as water, ρ=1000 kg/m^3). The normalized residual error (RMS error divided by RMS displacement) of the fit was also stored for each point. Voxels assumed to be corrupted by edge artifacts from numerical differentiation and Helmholtz decomposition were omitted. Finally, although Eq. (6) applies to each direction of motion, we used the lateral (phase-encode) component exclusively, since contrast-to-noise ratio was significantly higher in that direction. The analysis was carried out using custom routines implemented in Matlab™ (The Mathworks, Natick, MA).

Validation

Gel Phantom—Gel "phantom" experiments were used to compare estimates of shear modulus obtained by MRE to estimates obtained by standard rheometry. Gelatin (Knox, Camden, NJ) was prepared at three concentrations to provide samples with different stiffness: Gel 1: 0.0288 g/ml of water; Gel 2: 0.0576 g/ml of water; Gel 3: 0.0720 g/ml of water. Each gel preparation was used to make one gel sample for elastography and one gel sample for rheometry. The gel phantom for elastography was a 20 mm × 20 mm × 20 mm cube of gelatin prepared and held in a Delrin™ container.

The dynamic shear modulus of each of the three gel preparations was independently measured with a shear plate rheometer (AR2000, TA Instruments, Delaware). One sample (1 mm thick, 40 mm in diameter) of each gel preparation was subjected to oscillatory shear deformation (5%) at 80 Hz between parallel plates at 20°C. Four tests per sample were performed to confirm stability and repeatability of measurements. The relationship between amplitude and phase harmonically-varying shear strain, $\varepsilon = \tilde{\varepsilon}\, e^{j\omega t}$, and shear stress, $\sigma = \tilde{\sigma}\, e^{j\omega t}$ can be written in terms of complex coefficients as,

$$\tilde{\sigma} = \mu (1 + j\eta)\, \tilde{\varepsilon} \tag{10}$$

where μ is the dynamic shear modulus at frequency ω, and η is the dimensionless loss factor.

Estimates of the complex shear modulus found by rheometry at 80 Hz are shown in Table 1. Although shear modulus was controlled by varying gelatin concentration, the shear modulus varies with temperature, and also with storage time, which affects the amount of polymer cross-linking in the gel. All samples were stored for 18 hours at 10°C before equilibrating for 30 minutes at 20°C, to mimic the treatment of gel samples used in MRE experiments.

For MRE experiments in gel, the gel was molded inside a custom-built Delrin container. The container was held in the stereotaxic holder, and the actuator tip was placed on a plastic disk on the open surface of the gel. Typical acquisition parameters were similar to those used for the mouse: repetition time t_r = 1 s; echo time t_e=34 ms; 64 × 64 data matrix; field of view 32 mm × 32 mm; slice thickness of 0.5 mm (voxel size of 0.5 × 0.5 × 0.5 mm). For studies at 80 Hz, t_e=69 ms was used. Data were interpolated to 0.25 × 0.25 × 0.25 mm for analysis and presentation. The upper surface of three gel phantoms were vibrated laterally (horizontally) at 80, 200, 400, and 800 Hz. The MRE pulse sequence was used to visualize motion; two, two, four, and eight cycles of the motion-sensitizing gradients were applied on each side of the 180° pulse. The gel phantom data was analyzed with the same processing algorithm as the mouse brain data.

Finite Element Simulation—FE simulations were used to provide independent data from a system with known shear modulus, to evaluate the elastography method. Simulated data sets were generated from a FE model of a general 3-D, isotropic, linear, viscoelastic solid. The commercial package COMSOL™ (Burlington, MA) was used.

Although our primary goal was not to reproduce the response of the gel phantoms, we used shear modulus similar to that of Gel 2 (1600 N/m^2) and a "typical" loss factor (0.1) to create realistic simulations. These values were used at all frequencies in the FE simulation. The gel was assumed to be almost incompressible (Poisson's ratio $\nu = 0.49$) with a density of 1000 kg/m^3. Boundary conditions restricting displacement normal to the sides of the container were imposed, and sinusoidal forcing (80 Hz, 200 Hz, 400 Hz, or 800 Hz) was applied tangent to the top surface. The baseline FE model contained 15,235 quadratic tetrahedral elements and 3372 nodes arranged in a 25 mm × 25 mm × 6.25 mm rectangular volume with an element volume ratio of 0.038. Simulations of 80 Hz waves were also done in an enlarged domain containing 22564 quadratic tetrahedral elements and 5041 nodes arranged in a 50 mm × 50 mm × 6.25 mm rectangular volume. This discretization was obtained by refining the mesh until results converged (defined for our purposes by convergence of shear wavelength). The FE displacement data was analyzed with the same processing algorithm used on the MRE data, beginning with the Helmholtz decomposition.

Global, approximate, estimate of shear modulus

To check our shear modulus estimates, a rough calculation was performed for each data set using Eq. (8), rewritten below as

$$\mu_{approx} = \frac{\rho\omega^2}{k_{approx}^2} \tag{11}$$

where $k_{approx} = 2\pi/\lambda_{approx}$ is the approximate spatial frequency, estimated from the wavelength in the superior-inferior (readout) direction, which was the dominant direction of propagation.

RESULTS

Validation

Images of displacement in the gel phantom (Gel 2) excited at 400 Hz appear in Fig. 4. The figure shows motion in the readout, phase-encode, and slice-select direction for one section at four equally spaced times in the excitation cycle. The proportionality constant relating displacement to phase in the gel experiments (Eq. (2)) was $C=12.5$ μm/radian. The mechanical excitation is in the phase-encode (horizontal) direction.

Analogous displacement images from FE simulation are shown in Fig. 5. Displacement images are obtained by interpolating steady-state displacements from the FE mesh onto a 64×64×16 array of "voxels". These images are displayed at four equally spaced time points during the excitation period. Shear modulus and normalized residual error maps, estimated from the wave data of Figs. 4 and 5, are shown in Fig. 6.

Low frequency, long-wavelength (2−3 waves/image and 16−30 voxels/wave) behavior in gels and FE simulations approximates the conditions observed in the mouse brain at 1200 Hz. Data from Gel 1 excited at 80 Hz, Gels 2 and 3 excited at 200 Hz, and FE simulations of 1600 N/m^2 gel at 80 Hz and 200 Hz were examined carefully using both methods of Laplacian estimation. Figure 7(a) shows 200 Hz waves in Gel 2, along with the corresponding shear modulus and residual error estimates. The estimates in Fig. 7 were obtained with Laplacian estimated by the frequency-domain method. The maps of shear modulus and residual error in Fig. 7(b-c) include edge effects attributable to Helmholtz decomposition and Laplacian estimation. After masking out affected voxels (within 4 voxels of edges), the mean±std. dev. shear modulus was 1460±20 N/m^2, which is close to the value obtained by shear plate rheometry at 80 Hz (1550 N/m^2, see Table 1). The corresponding estimate using a finite-difference Laplacian was 1680±140 N/m^2. Numerical values of estimated shear modulus for the gel phantom experiments and FE simulations appear in Table 2. For long wavelength data,

both methods of Laplacian estimation were used; results obtained with finite difference estimate of the Laplacian are shown in parentheses in Table 2.

Summary data from all three gel samples and FE simulations are shown in Fig. 8. Figure 8(a) shows shear modulus estimates from all gel experiments and estimates obtained by shear plate rheometry at 80 Hz. For MRE the mean and standard deviation were obtained from ~1500 individual voxel-wise estimates in one gel sample; rheometry data are from four repeated tests on a corresponding sample from the same gel preparation The dynamic shear modulus estimate increases with frequency due to the viscoelastic nature of the gel. The mean MRE estimate of shear modulus obtained at 200 Hz in the stiffest gel (Gel 3) was within 14% of the value obtained by rheometry at 80 Hz. (2560 N/m^2 for MRE vs 2980 N/m^2 for rheometry). In Gel 2 the difference was 6% (1460 N/m^2 vs 1550 N/m^2). In Gel 1 the difference was 34% (290 N/m^2 vs 440 N/m^2). The relationship between mean rheometry and mean elastography estimates for the three gels is well-modeled by the linear function $\mu_{RH} = 1.12\mu + 52$ (R^2=0.99).

Fig.8(b) summarizes the results from FE simulation. All estimates from FE simulations are within 10% of each other and the input parameter of μ = 1600 N/m^2 (note dynamic shear modulus is held fixed in the FE simulation, and does not increase with frequency).

We conclude that for long wavelength data characteristic of our mouse experiments, (spatial resolution of > 16 voxels/wave and at least 2 wavelengths/domain) the elastography approach works reliably, although the spatial resolution is limited by wavelength and estimates near edges are unavailable. In the short-wavelength regime (< 16 voxels/wave; 400−800 Hz in Gels 2 and 3; 200 Hz in Gel 1) the frequency-domain method is preferable, because it is less sensitive to sampling rate. At short wavelengths edge effects are much less significant and spatial resolution of shear modulus estimates is higher.

Mouse Brain

Images of mouse brain coronal sections at four time points showing transverse (shear) displacement due to wave motion in the phase-encode (PE; lateral) direction appear in Fig. 9. The middle section is taken approximately at the level of the anterior hippocampus. The anterior and posterior slices were 3 mm in front and 2 mm behind the middle slice, respectively. Fig. 10 shows transverse displacement in the middle section in the readout (RO; inferior-superior), phase-encode (PE; lateral), and slice-select (SS; anterior-posterior) directions. The mechanical excitation was in the horizontal (phase-encode) direction. The proportionality constant (Eq. (2)) used to estimate displacement from phase was C=7.5 μm/radian.

Estimates of dynamic shear modulus and normalized residual error appear in Fig. 11, along with corresponding anatomical images of the anterior, middle, and posterior sections of the mouse brain. In locations where the normalized residual error was greater than 0.5, the estimate of shear modulus was judged to be unreliable and was dropped. These conditions seem to arise in regions where destructive interference leads to small displacement amplitudes and low signal-to-noise ratios.

Mean values of dynamic shear modulus estimates were obtained in the cortical gray matter of anterior, middle and posterior mouse brain sections (typically N=1200−1900 voxels) for six animals in vivo (Fig. 12). Regions of white matter in the mouse are much smaller than the average wavelength, and separate estimates of shear modulus in white matter could not be obtained. Error bars in Fig. 12 represent the standard deviation of all of the shear modulus estimates found in the region of interest (i.e., cortical gray matter, slice region). The middle section is taken approximately at the level of the anterior hippocampus. The anterior and posterior slices were 3 mm in front and 2 mm behind the middle slice, respectively. In the

mouse, the gross anatomical regions of interest (i.e., cortical and sub-cortical gray matter) are readily identified on anatomical images, and transferred to shear modulus images.

Analogous results for sub-cortical gray matter appear in Fig. 13. Figure 14 shows dynamic shear modulus estimates in cortical and sub-cortical gray matter for two mice imaged *post mortem*. All estimates of shear modulus are similar in both living and dead tissue. No difference was found to be statistically significant (Student's t-test).

DISCUSSION

MRE allows visualization of shear wave motion and estimation of dynamic elastic parameters. This method can be used non-invasively to assess properties of the entire brain. In the current study, this method was applied to measure mechanical properties of the mouse brain *in vivo* for the first time, at a frequency (1200 Hz) significantly higher than previously reported for *in vivo* MRE [11,14].

A simple isotropic, linear elastic model was used to interpret measurements of displacement during wave propagation. The isotropic model contains the assumption that the shear wave speed is approximately independent of direction. In reality, some brain tissues of large mammals, especially the brain stem and white matter tracts, have been found to be anisotropic in *ex vivo* tests [7]. However, even at 1200 Hz, each wavelength is larger than the typical anisotropic structure in the mouse brain. Therefore, significant averaging of properties is expected, and results are expected to be generally similar in all directions.

Displacements were measured in all three directions during horizontal (lateral) vibration of the skull. However, the largest displacements were in the lateral (phase-encode) direction, providing higher contrast-to-noise than in the other directions. For this reason the shear modulus estimates were calculated from the displacement data in the phase-encode direction.

The major challenge in data analysis is accurate estimation of the second derivatives used to calculate the Laplacian. Differentiation can be done in the space domain or in the spatial frequency domain. We used both approaches, and compared results in gels and FE simulations. Each method has potential sources of error. For long wavelengths relative to the domain size, the spatial frequency ($k=2\pi/\lambda$) is close to the fundamental frequency of the discrete Fourier transform ($2\pi/L$). Errors may arise in frequency-domain approaches, due to the lack of frequency resolution, as well as to truncation artifacts [21]. For short wavelengths, lack of spatial resolution may lead to underestimation of the Laplacian by finite difference methods. Possible solutions include interpolation, spatial filtering [14], or local polynomial fitting [17]. As described above, we estimated the Laplacian with simple versions of both a finite difference method (for long wavelength data) and frequency domain method (preferred for short wavelength data). For MRE in the mouse, we estimated the Laplacian by a smoothed finite difference method, because spatial resolution was high and there were few wavelengths.

Results from gel phantoms and FE simulations provide evidence that the elastography method is quite accurate over a wide range of practical frequencies in gel and gel-like materials. The strongest evidence for the accuracy of the method is from MRE analysis of data from FE simulations, in which the true shear modulus is known for all frequencies. Estimates from FE simulation were always within 10% (mean error = 5.3%) of the input parameter μ = 1600 N/m^2. In the two stiffer gels, the MRE estimates of shear modulus at 200 Hz and rheometry estimates at 80 Hz were within 15%; in the very soft gel (Gel 1, μ_{RH} = 440 N/m^2) the difference was 34%. In this soft gel, a relatively small absolute difference between estimates of gel shear modulus obtained by MRE and rheometry at 80 Hz represented a relatively large percent difference because the gel had a very low modulus. The lack of precise temperature control in the bore of the MR scanner almost surely contributed to this difference. MRE studies were

performed at room temperature, which varied between 20−23°C. Rheometry tests were performed with precise temperature control at 20°C±0.1C. The gel modulus is very sensitive to temperature and the difference of a few degrees (23°C vs 20°C) could account for the lower estimate of shear modulus obtained by MRE.

The relationship between moduli from rheometry and MRE was fitted well by a linear function with slope near one and intercept near zero. Again, differences from perfect agreement (unit slope, zero intercept, $R^2=1$) may be partly attributable to temperature variations of a few degrees Celsius during imaging. Estimates of shear modulus were also checked with an approximate calculation based on wavelength in one direction.

Dynamic shear moduli were estimated by fitting the wave equation to observed displacement fields. Relatively high residual errors for this fit were found in the center of the anterior and middle sections. Observations of wave motion suggests that destructive wave interference in this region leads to very low-amplitude waves and thus a low signal-to-noise ratio. Estimates of shear modulus in regions with high residual error were discarded.

It is important to note that the estimates for the mouse brain are of the *dynamic* shear modulus at the specific frequency used: 1200 Hz. In the gel phantom, different frequencies of excitation yielded different values of dynamic shear modulus. This behavior is an inherent property of both gels and biological tissues. In theory, data from the mouse brain could be fitted to a fully viscoelastic model of wave propagation. In practice, viscoelasticity was not modeled because the brain images did not contain enough wavelengths at 1200 Hz to allow estimation of decay parameters. It was also impractical to vary the frequency because at lower frequencies, the wavelength approaches and exceeds the size of the mouse brain, and at frequencies higher than 1200 Hz the amplitude of motion decreases rapidly.

The shear modulus estimates in Table 3 suggest slightly higher stiffness in the anterior section of the brain than in the posterior section analyzed. The results also suggest higher stiffness in the sub-cortical gray matter of the mouse brain than in the cortical gray matter. These trends are not statistically significant in these animals, largely because of scatter in the experimental measurements at these spatial resolutions.

Future work will focus on application of this technique in a larger animal model, including measurement of anisotropic and viscoelastic properties at multiple frequencies. Sinkus and co-workers [17] have employed an anisotropic model to study breast tumors. We expect that their approach will be feasible for brain tissue at larger scales.

The shear moduli found for mouse brain in this study at 1200 Hz (12,000−19,000 N/m^2) are higher than those measured by McCracken et al. [15] in a single human brain at 200 Hz (5,000 −11,000 N/m^2). This is highly consistent with the expected increase of dynamic shear modulus with frequency; it is also possible that mouse brain is stiffer than human brain. Estimates of dynamic shear modulus reported here are also higher than those reported by Gefen and Margulies in the porcine brain *in vivo* [8] (685−1875 N/m^2),. Their results were obtained at lower frequencies, under conditions in which the skull was opened. Miller et al. [22] tested porcine brain in axial tension and estimated the instantaneous shear modulus for small strain to be 842 Pa. Brands and colleagues [23] subjected porcine brain to 1% shear strain at frequencies up to 16 Hz, and then used the “time-temperature superposition principle” to estimate the dynamic shear modulus at just below 1000 Hz to be approximately 2000 Pa. Bilston et al. [24] estimated the complex shear modulus of bovine brain samples undergoing small oscillatory shear 0.1% strain. They estimate a complex shear modulus of approximately $5000+i500$ Pa at 10 Hz [24]. Differences may be attributable in part to the specimen tested (porcine or bovine instead of murine) and the frequencies used. Finally, estimates of dynamic shear modulus reported here are slightly higher than that those reported by Darvish and Crandall

[9] at 200 Hz (~10,000 N/m^2); the difference may again be attributable to the frequency range used.

In conclusion, the current study demonstrates the use of MRE to characterize the mechanical properties of mouse brain tissue. This study highlights the importance of frequency (or deformation rate) on the apparent shear modulus found by MRE. This rate-dependence is very important for studies of brain trauma, in which deformation occurs over intervals of milliseconds or less. The current estimates of material properties, which strictly apply to small deformations at 1200 Hz, are obtained throughout the brain and may be used to complement or scale estimates of nonlinear properties obtained *ex vivo* or by invasive methods.

ACKNOWLEDGEMENTS

We gratefully acknowledge the assistance of Benjamin Zatlin, Christine MacDonald and colleagues in the Washington University Biomedical MR Laboratory. MRI facilities support was provided by National Cancer Institute Small Animal Imaging Resource (SAIR) Program grant R24-CA83060: the Washington University Small Animal Imaging Resource (WUSAIR). Support from the NIH grant NS45237 and from the McDonnell Center for Higher Brain Function at Washington University is acknowledged.

REFERENCES

1. Srinivasan S, Krouskop T, Ophir J. A quantitative comparison of modulus images obtained using nanoindentation with strain elastograms. Ultrasound in Medicine and Biology 2004;30(7):899–918. [PubMed: 15313323]
2. Xie H, Kim K, Aglyamov SR, Emelianov SY, O'Donnell M, Weitzel WF, Wrobleski SK, Myers DD, Wakefield TW, Rubin JM. Correspondence of Ultrasound Elasticity Imaging to Direct Mechanical Measurement in Aging DVT Rats. Ultrasound in Medicine & Biology 2005;31(10):1351–1359. [PubMed: 16223638]
3. Techavipoo U, Chen Q, Varghese T, Zagzebski JA. Estimation of Displacement Vectors and Strain Tensors in Elastography Using Angular Isonifications. IEEE Transactions on Medical Imaging 2004;20(12):1479–1489. [PubMed: 15575406]
4. Bayly PV, Cohen TS, Leister EP, Ajo D, Leuthardt EC, Genin GM. Deformation of the Human Brain Induced by Mild Acceleration. Journal of Neurotrauma 2005;22(8):845–856. [PubMed: 16083352]
5. Bayly PV, Black EE, Pedersen RC, Leister EP, Genin GM. *In vivo* measurement of rapid deformation and strain in an animal model of traumatic brain injury. Journal of Biomechanics 2006;39(6):1086–1095. [PubMed: 16549098]
6. Margulies SS, Thibault LE, Gennarelli TA. Physical Model Simulations of Brain Injury in a Primate. Journal of Biomechanics 1990;23(8):823–836. [PubMed: 2384494]
7. Prange MT, Margulies SS. Regional, Directional, and Age-Dependent Properties of the Brain Undergoing Large Deformation. Journal of Biomechanical Engineering 2002;124(2):244–252. [PubMed: 12002135]
8. Gefen A, Margulies SS. Are *in vivo* and in situ brain tissues mechanically similar? Journal of Biomechanics 2004;37(9):1339–1352. [PubMed: 15275841]
9. Darvish KK, Crandall JR. Nonlinear viscoelastic effects in oscillatory shear deformation of brain tissue. Medical Engineering & Physics 2001;23:633–645. [PubMed: 11755808]
10. Van Essen D. A Tension-Based Theory of Morphogenesis and Compact Wiring in the Central Nervous System. Nature 1997;385(6614):313–318. [PubMed: 9002514]
11. Othman SF, Xu H, Royston TJ, Magin RL. Microscopic Magnetic Resonance Elastography (μMRE). Magnetic Resonance in Medicine 2005;54(3):605–615. [PubMed: 16088876]
12. Muthupillai R, Lomas DJ, Rossman PJ, Greenleaf JF, Manduca A, Ehman RL. Magnetic Resonance Elastography by direct Visualization of Propagating Acoustic Strain Waves. Science September 29;1995 269(5232):1854–1857. [PubMed: 7569924]
13. Romano AJ, Bucaro JA, Ehman RL, Shirron JJ. Evaluation of a Material Parameter Extraction Algorithm Using MRI-Based Displacement Measurements. IEEE transactions on Ultrasonics, Ferroelectrics, and Frequency Control 2000;47(6):1575–1581.

14. Manduca A, Oliphant TE, Dresner MA, Mahowald JL, Kruse SA, Amromin E, Felmlee JP, Greenleaf JF, Ehman RL. Magnetic Resonance Elastography: Non-invasive Mapping of Tissue Elasticity. Medical Image Analysis 2001;5:237–254. [PubMed: 11731304]
15. McCracken PJ, Manduca A, Felmlee J, Ehman RL. Mechanical Transient-Based Magnetic Resonance Elastography. Magnetic Resonance in Medicine 2005;53(3):628–639. [PubMed: 15723406]
16. Romano AJ, Abraham PB, Rossman PJ, Bucaro JA, Ehman RL. Determination and Analysis of Guided Wave Propagation Using Magnetic Resonance Elastography. Magnetic Resonance in Medicine 2005;54(4):893–900. [PubMed: 16155879]
17. Sinkus R, Tanter M, Catheline S, Lorenzen J, Kuhl C, Sondermann E, Fink M. Imaging Anisotropic and Viscous Properties of Breast Tissue by Magnetic Resonance-Elastography. Magnetic Resonance in Medicine 2005;53(2):272–387.
18. Plewes DB, Silver S, Starkoski B, Walker CLJ. Magnetic Resonance Imaging of Ultrasound Fields: Gradient Characteristics. Journal of Magnetic Resonance Imaging 2000;11(4):452–457. [PubMed: 10767075]
19. Lopez, O.; Manduca, A.; Ehman, RL. Validation of a dynamic MR elastography technique customized for in vitro biomechanical assessment of articular cartilage under high frequency cyclical shear; ISMRM 14th Scientific Meeting.; Seattle, WA. 2006. #325
20. Fung, YC. A First Course in Continuum Mechanics. Prentice-Hall, Inc.; Englewood Cliffs: 1994. p. 271Chap. 12
21. Press, WH.; Flannery, BP.; Teukolsky, SA.; Vetterling, WT. Numerical Recipes in C. Cambridge University Press; New York: 1992.
22. Miller K, Chinzei K. Mechanical properties of brain tissue in tension. Journal of Biomechanics 2002;35(4):483–490. [PubMed: 11934417]
23. Brands DWA, Bovendeerd PHM, Peters GWM. The Large Shear Strain Dynamic Behaviour of In-Vitro Porcine Brain Tissue and a Silicone Gel Model Material. Stapp Car Crash Journal 2000;44:249–260. [PubMed: 17458730]
24. Bilston LE, Liu Z, Phan-Thien H. Large strain behavior of brain tissue in shear: Some experimental data and differential constitutive model. Biorheology 2001;38:335–345. [PubMed: 11673648]

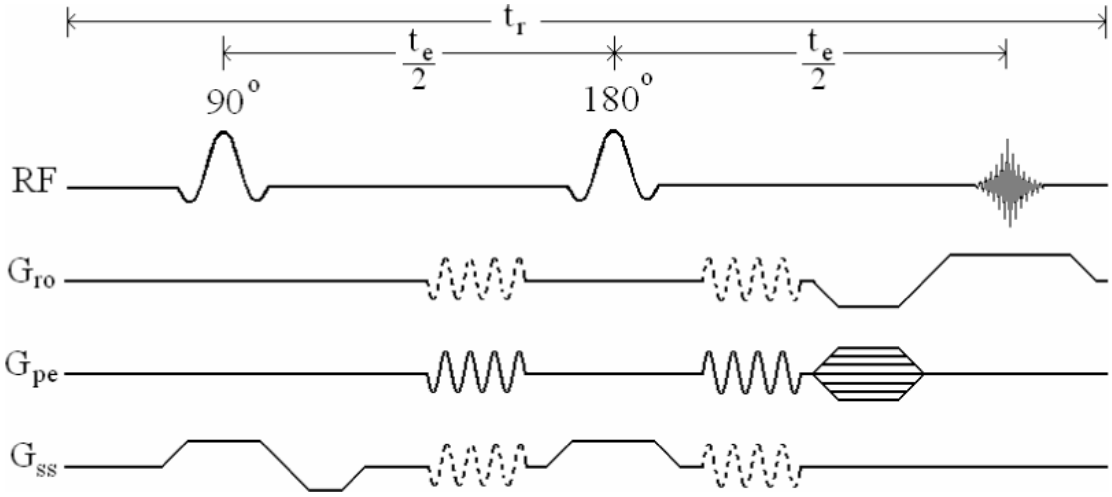

Figure 1.

The MR elastography pulse sequence. A standard spin-echo MR imaging sequence was modified by the addition of sinusoidal motion-sensitizing gradients that oscillate at the frequency of vibration. The basic spin-echo sequence consists of RF excitation in conjunction with gradients in the slice-select (G_{ss}), read-out (G_{ro}), and phase-encode (G_{pe}) directions. This figure depicts harmonic motion-sensitizing gradients in the phase-encode direction. The dashed lines indicate that motion sensitizing gradients could also be applied in the readout and slice-select directions.

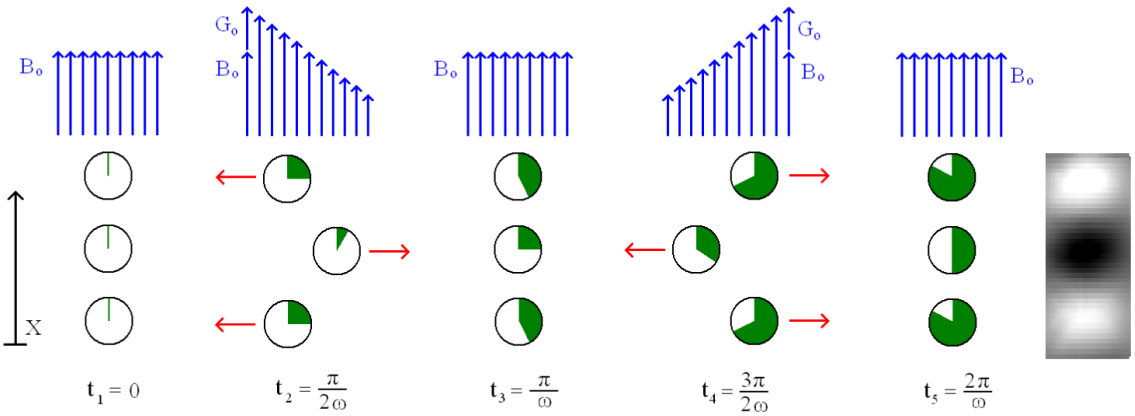

Figure 2.

Illustration of phase accumulation using MRE. The three rows of circles represent three individual “spin packets”, and the portion filled in represents the phase of a spin at a particular time. The five columns represent a complete cycle of vibration as well as gradient modulation of period $T=^{2\pi}/_{\omega}$ where the ω is the frequency of vibration measured in radians per second. The amount of phase that a spin accumulates at a given time is directly proportional to the magnetic field strength at that point. Thus at t_2 the upper and lower spins accrue more phase than the middle spin because they have been displaced by vibration into a higher magnetic field. At t_4 the spins are displaced in the opposite direction, however the gradient field has also switched direction and the upper and lower spins again accrue more phase than the middle spin. The net result is an image whose phase is proportional to displacement at a particular time during one cycle, as seen on the right. An image of the displacements at a different point in the cycle can be obtained by shifting the motion-sensitizing gradients temporally. Time series of periodic displacements (and animations of wave propagation) can be obtained by incrementally varying this temporal delay between the mechanical excitation and the imaging gradients.

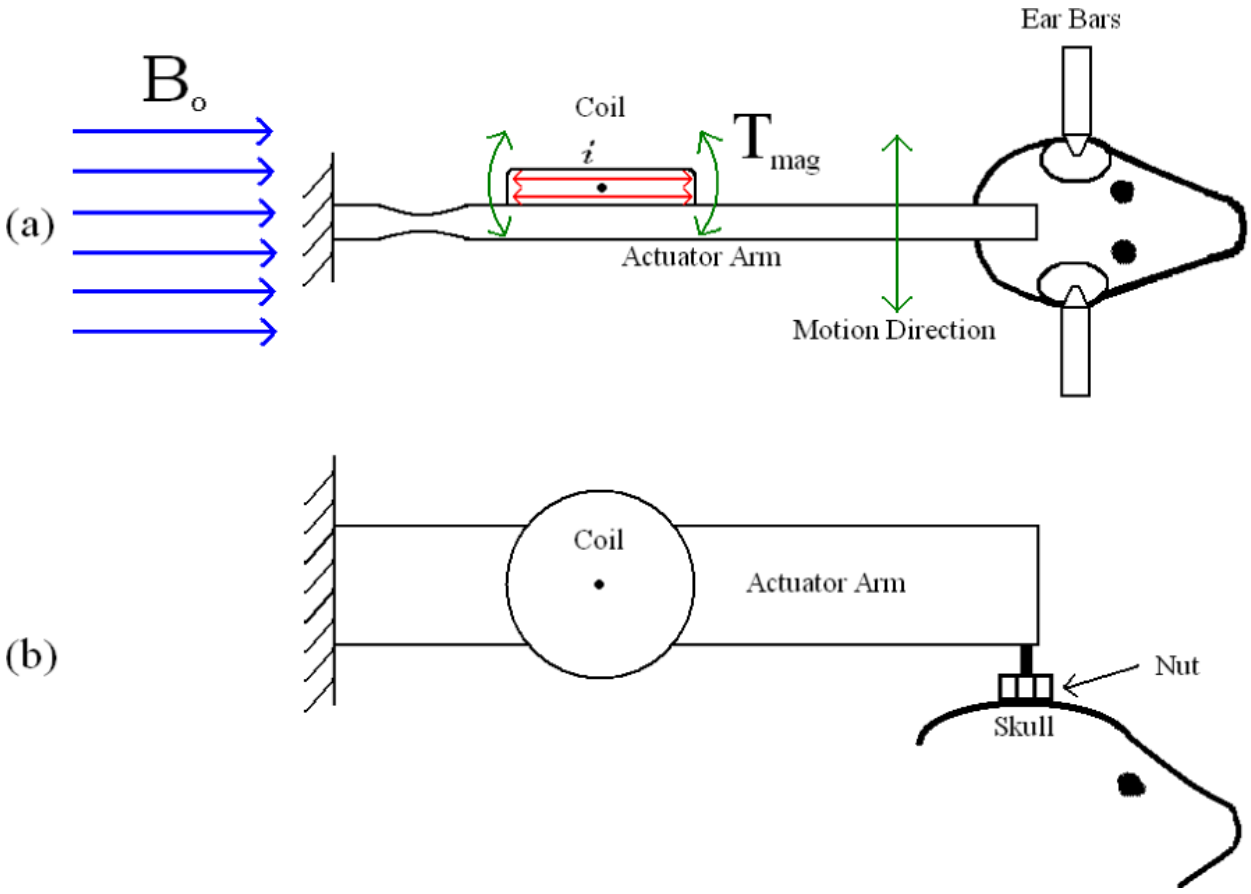

Figure 3.

(a) Top view of the wave-generating actuator. When a sinusoidal current, i, is sent through the coil in the longitudinal magnetic field, B_o, an electromagnetic torque, T_{mag}, is developed, causing the actuator arm to vibrate back and forth. (b) A side view of the shaker apparatus showing the connection between the arm and a plastic machine screw nut glued to the skull. The coronal imaging plane is perpendicular to both views.

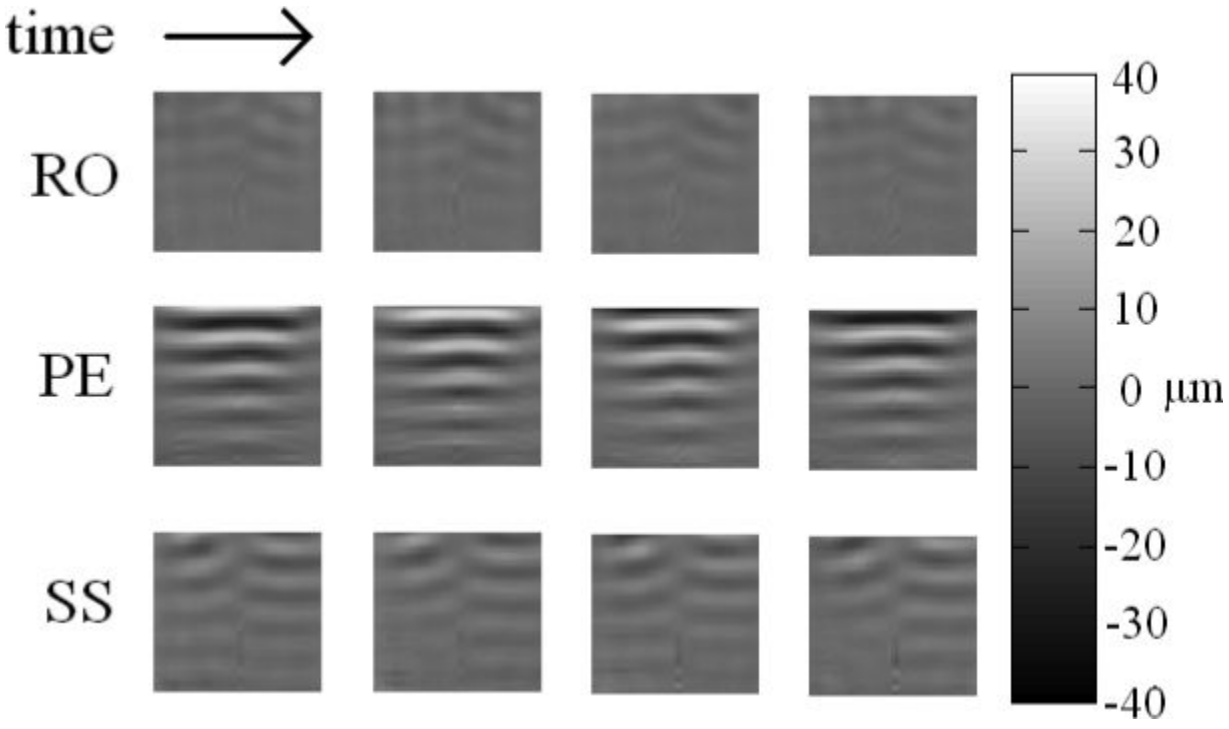

Figure 4.

MRE displacement images of a gel phantom (Gel 2) showing four time points in a complete cycle of wave motion at 400 Hz. Waves can be seen most clearly in the phase-encode (PE; lateral) direction, which was the direction of excitation. The maximum amplitude in the PE direction was 33 μm. Each frame is 18 mm × 17.5 mm. Directions are: RO – inferior-superior; PE - lateral; SS – anterior-posterior.

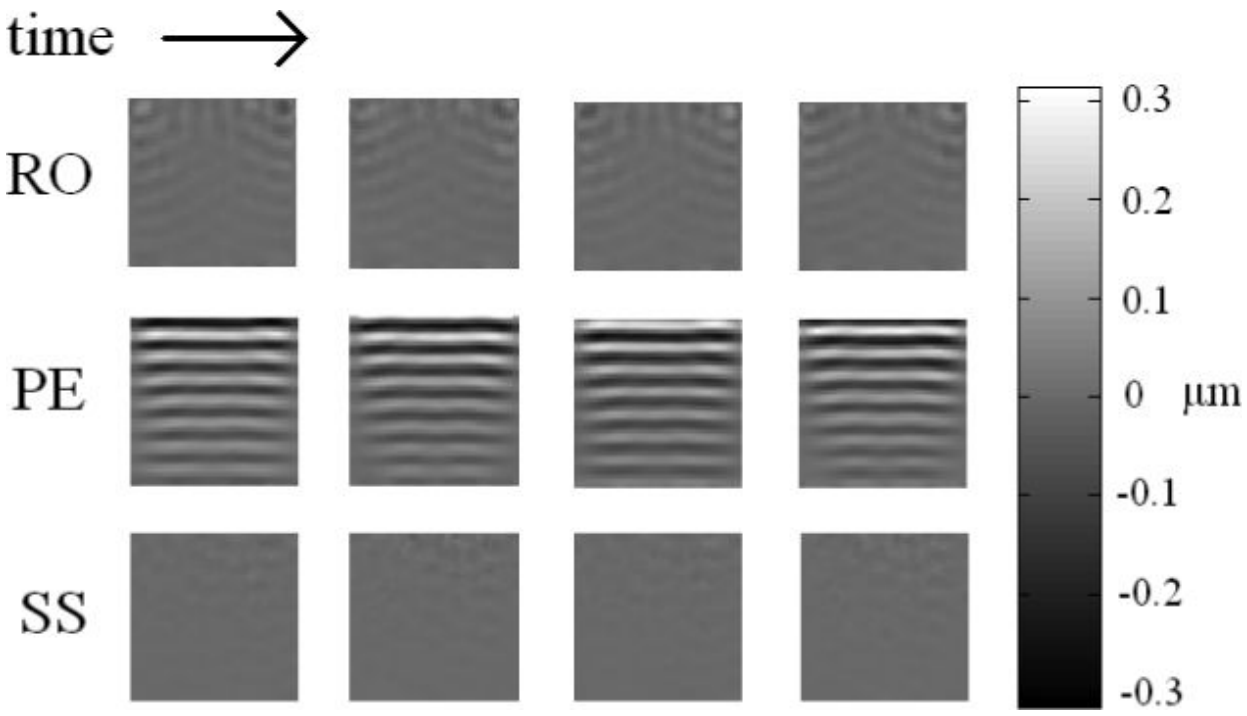

Figure 5.
Images of displacement from a FE simulation of shear wave propagation in a 3-D viscoelastic solid. Parameters: shear modulus $\mu = 1600$ N/m^2 ; loss factor $\eta = 0.1$; excitation frequency 400 Hz. Image size is 25 mm × 25 mm × 6.25 mm; displacements were interpolated onto an array of 64 × 64 × 16 “voxels”.

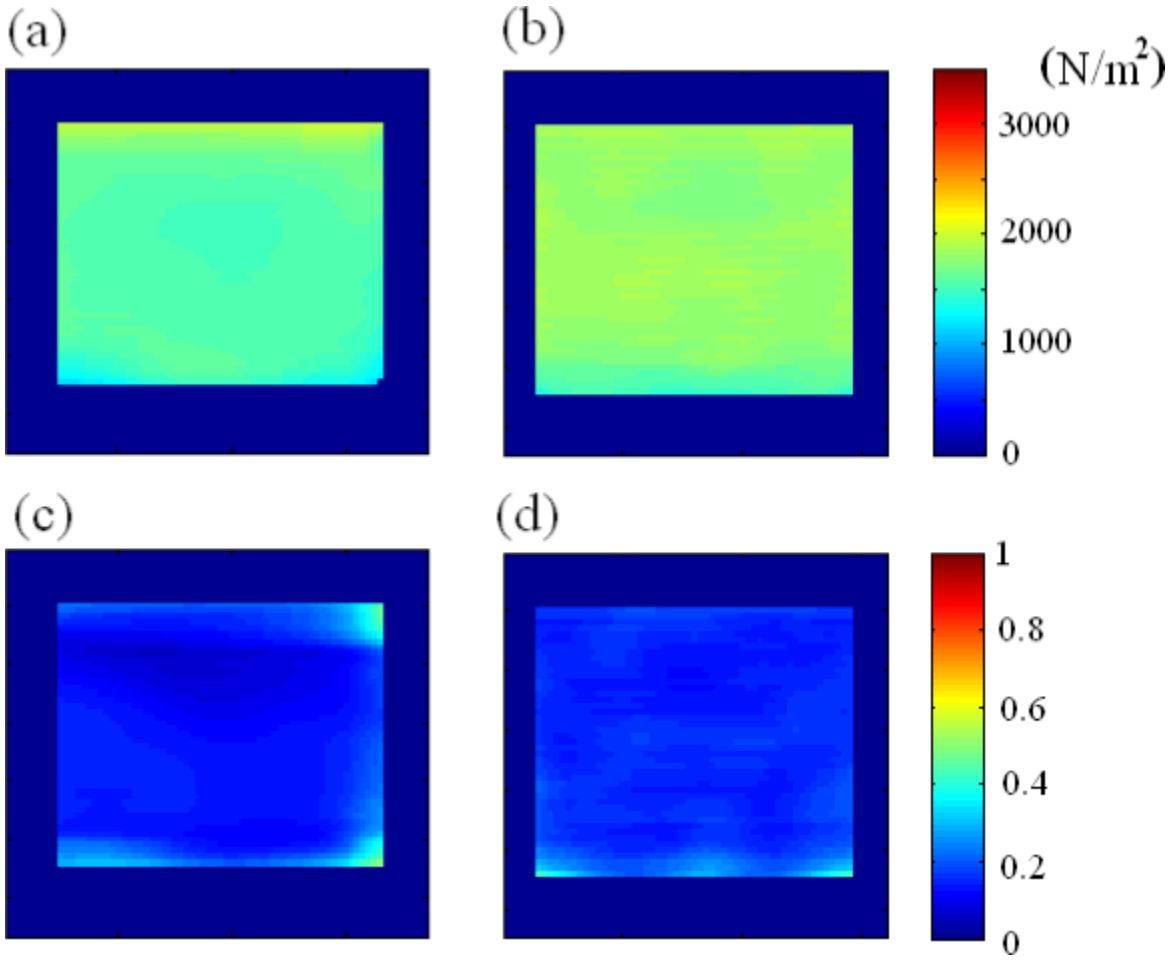

Figure 6.

Shear modulus estimates and residual error for data from 400 Hz excitation of gel phantom and FE simulation. Panel (a): Shear modulus estimate for Gel 2 (Fig. 4). The mean(±std. dev.) estimate was 1560±70 N/m^2.. Panel (b): Shear modulus estimate for the 400 Hz FE simulation (Fig. 5). The mean(±std. dev.) estimate is 1760±90 N/m^2. Panel (c): Residual error of wave equation fit for the gel phantom. (d) Residual error of wave equation fit for the FE simulation.

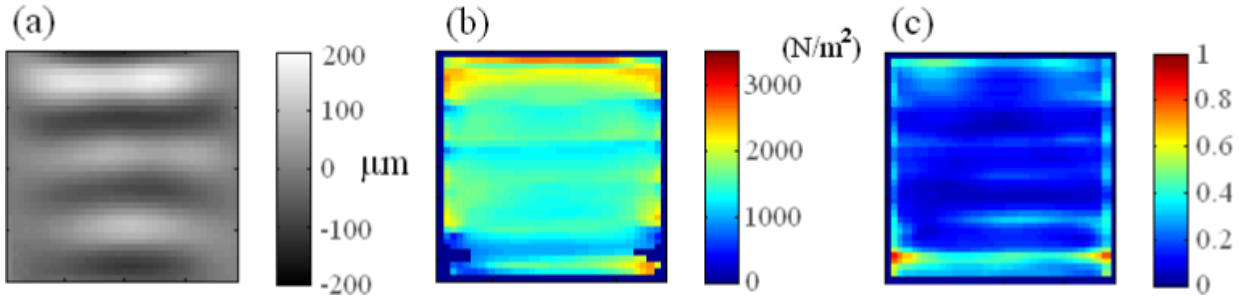

Figure 7.

(a) Waves in Gel 2 at 200 Hz; ~2.5 wavelengths/domain. (b) Map of shear modulus estimates, illustrating edge artifacts. (c) Map of residual error of fit to the wave equation, including edge artifacts. Edge effects are attributable to truncation error in Helmholtz decomposition and Laplacian estimation. With edge voxels masked out as in Fig. 6 above, the mean(±std. dev.) estimate was 1460±20 N/m^2 with the Laplacian estimated in the frequency domain (shown); 1680±140 N/m^2 with Laplacian estimated by finite differences in space.

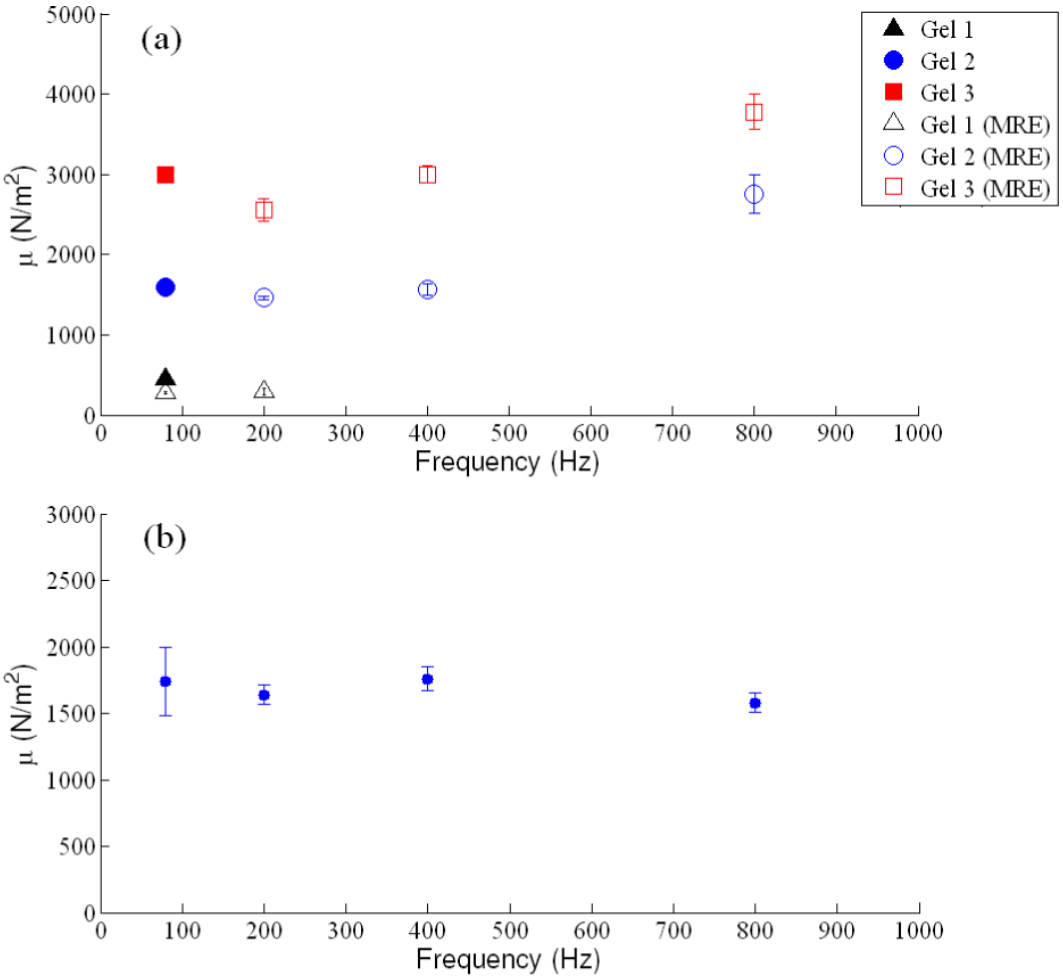

Figure 8.

Estimates of dynamic shear modulus for (a) gel phantoms and (b) FE simulations as a function of frequency. (a): Filled-in markers represent the shear moduli determined by shear plate rheometry at 80 Hz for three gel materials. Open markers represent the shear modulus estimates determined using MRE at 80, 200, 400, and 800 Hz. The gels exhibit frequency-dependent viscoelastic behavior; the dynamic shear modulus determined using elastography increases with increasing frequency. (b) Elastography estimates of shear modulus from FE simulations. Parameters: μ_0 = 1600 N/m^2; loss factor η = 0.1. Elastography yielded similar results for all frequencies of the FE model. Estimates are within 10% of each other, and are consistent with approximate values obtained from an estimate of wavelength in the RO direction (see Eq. (11), Table 2).

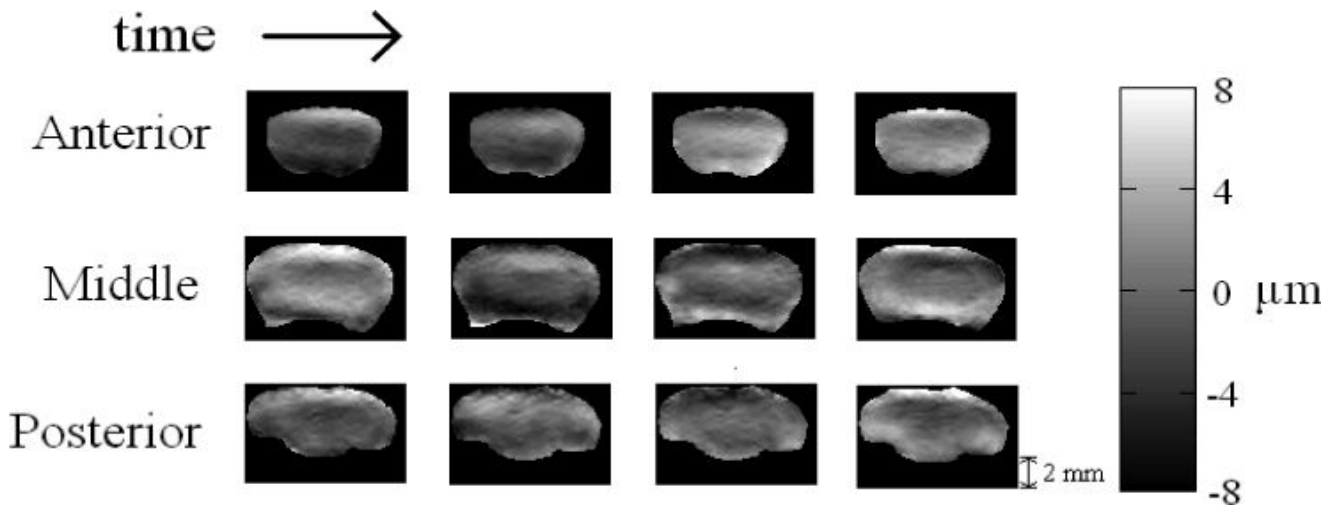

Figure 9.

MRE images of displacement in the phase-encode (PE; lateral) direction in anterior, middle, and posterior mouse brain sections at four points in time during a cycle of wave propagation at 1200 Hz. Excitation was in the PE direction. The maximum amplitude in the PE direction was approximately 10 μm. Each frame is 11.25 mm × 7.5 mm.

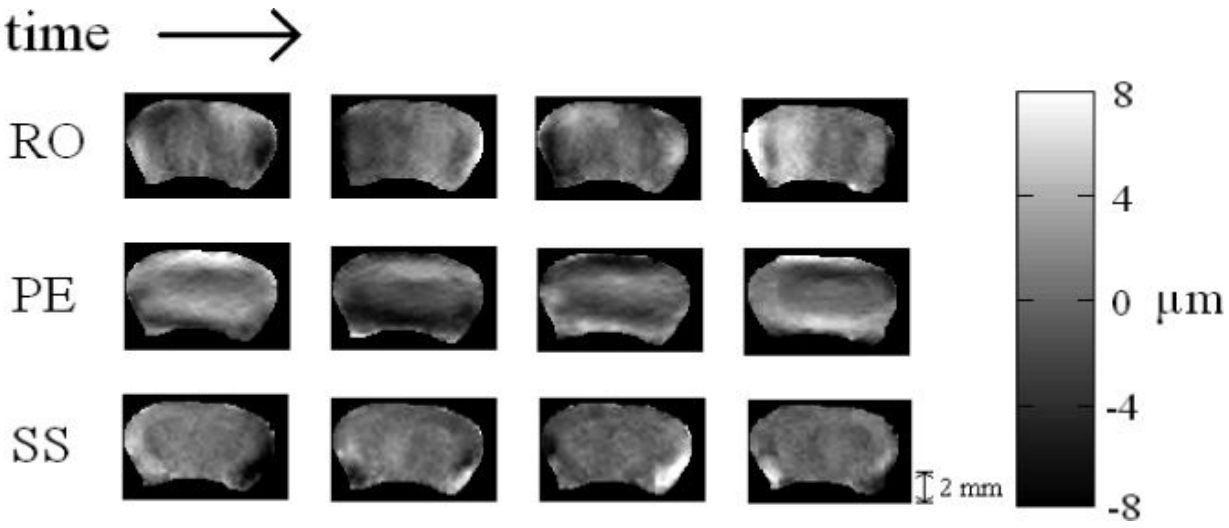

Figure 10.

MRE images of displacement in a mid-coronal mouse brain section showing four points in time during a cycle of wave propagation at 1200Hz with motion in all three directions. The maximum amplitude in the PE direction was ~10 μm. Each frame is 11.25 mm × 7.5 mm. Directions are: RO – inferior-superior; PE - lateral; SS – anterior-posterior.

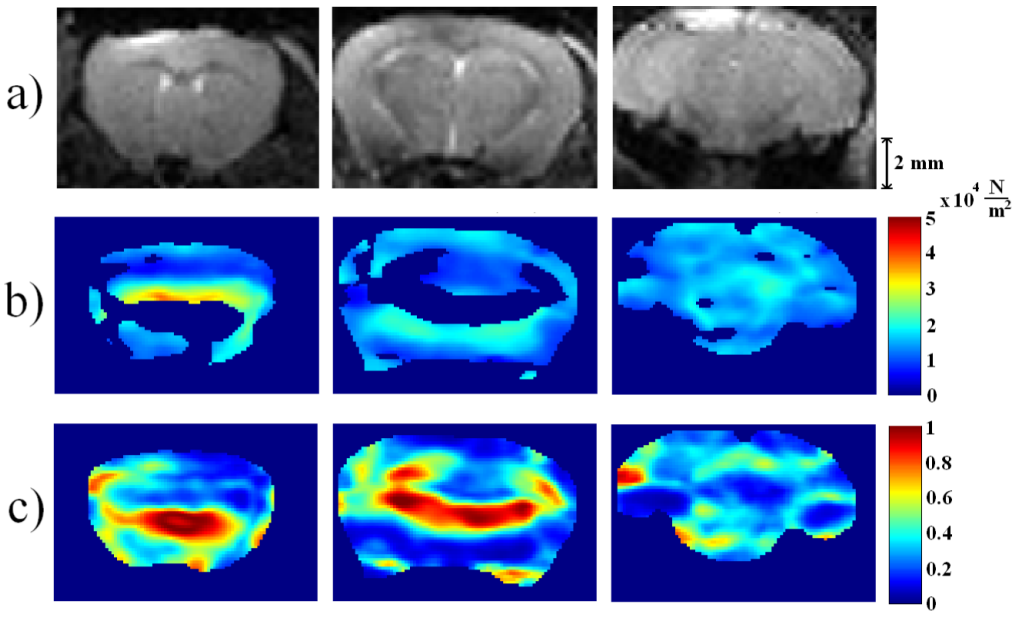

Figure 11.
Dynamic shear modulus in anatomical sections. (a) Spin echo “scout” images of anterior, middle, and posterior coronal sections of the mouse brain. (b) Representative images of dynamic shear modulus. Areas with residual error higher than 0.5 are masked out (dark blue). (c) Residual errors from the fit to the wave equation. Each frame is 11.25 mm × 7.5 mm.

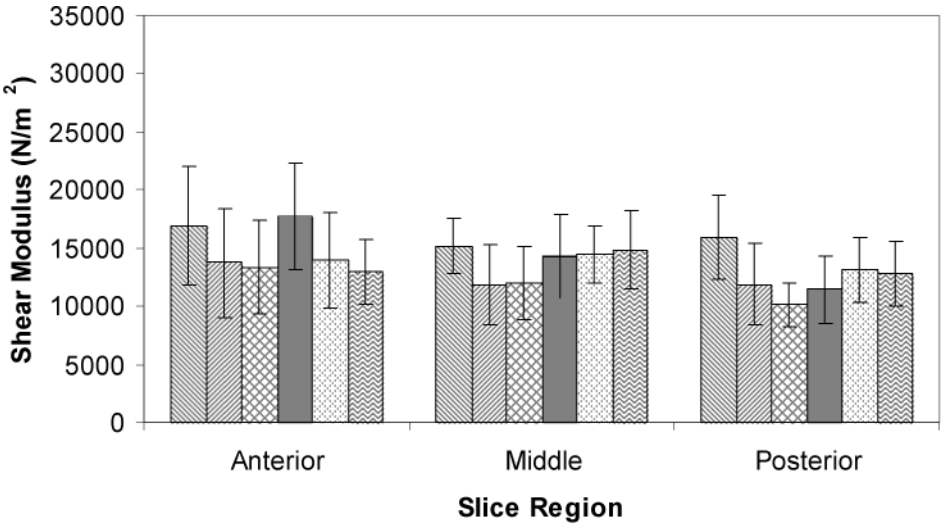

Figure 12.

Dynamic shear modulus estimates (mean±std. dev.) in the cortical gray matter of anterior, middle and posterior mouse brain sections for six animals *in vivo*. Each bar shading represents a single mouse. The average estimates of the shear modulus of all six mice in the anterior, middle, and posterior sections were 14800±2030 N/m^2, 13800±1490 N/m^2, and 12600±1990 N/m^2 respectively.

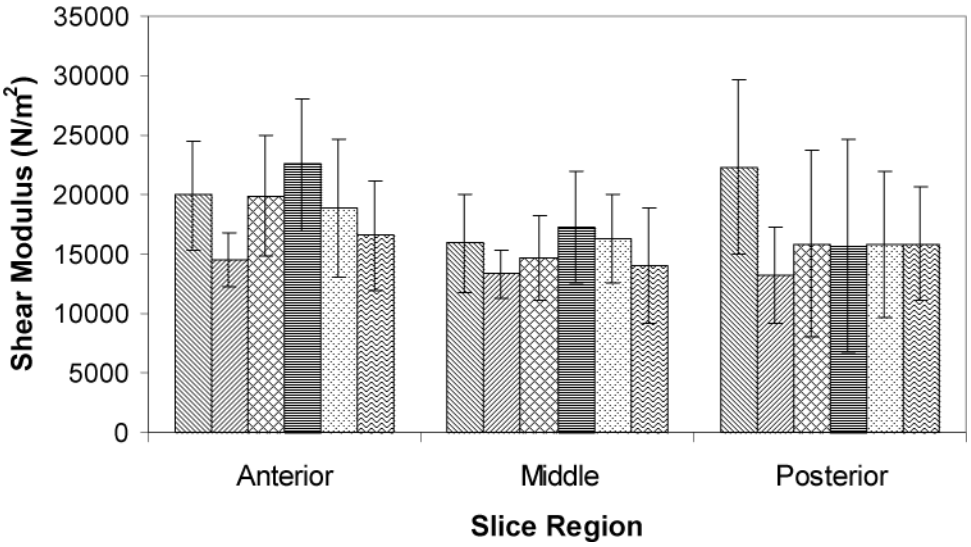

Figure 13.

Dynamic shear modulus estimates (mean±std. dev.) in the sub-cortical gray matter in anterior, middle and posterior mouse brain sections for six animals *in vivo*. Each bar shading represents one mouse. The average estimates of the shear modulus of all six mice in the anterior, middle, and posterior sections were 18700±2080, 15300±1480, and 16500±3060 N/m^2 respectively.

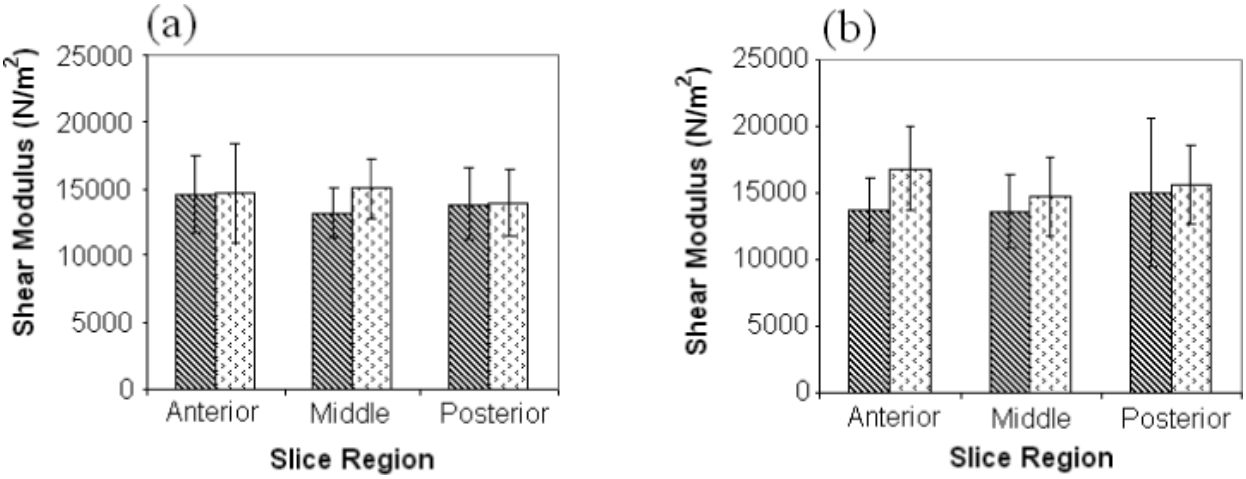

Figure 14.

Dynamic shear modulus estimates (mean±std. dev.) in anterior, middle, and posterior mouse brain sections for two animals *post mortem*. Each bar represents a single mouse. a) Cortical gray matter. The average estimates of the shear modulus of both mice in the anterior, middle, and posterior sections were 14600±50, 14100±1290, and 13900±70 N/m^2 respectively. b) Sub-cortical gray matter. The average estimates of the shear modulus of both mice in the anterior, middle, and posterior sections were 15400±2180, 14200±800, and 15400±410 N/m^2 respectively. No estimate of shear modulus was significantly different from the corresponding value observed in living tissue (Student's t-test).

TABLE 1

SHEAR MODULUS μ AND LOSS FACTOR η MEASURED BY RHEOMETRY AT 80 HZ FOR THREE GEL MATERIALS.

	Gel 1	Gel 2	Gel 3
μ (N/m^2)	**440**±10	**1550** ±1	**2980** ± 68
η	**0.09**±0.005	**0.20**±0.02	**0.04**±0.01

TABLE 2

DYNAMIC SHEAR MODULUS OF GELS AND FE SIMULATIONS ESTIMATED BY ELASTOGRAPHY (VALUES IN PARENTHESES OBTAINED WITH FINITE DIFFERENCE ESTIMATE OF LAPLACIAN).

		80 Hz	200 Hz	400 Hz	800 Hz
Gel 1 μ_{RH} = **440**±10 N/m^2	μ (N/m^2)	**280** ± 15 (**315** ± 16)	**290** ± 36 ------	------ ------	------ ------
	μ_{approx}	300	300	------	------
Gel 2 μ_{RH} = **1550** ±1 N/m^2	μ (N/m^2)	------ ------	**1460** ± 20 (**1680** ± 140)	**1560** ± 70 ------	**2750** ± 240 ------
	μ_{approx}	------	1500	1800	3100
Gel 3 μ_{RH} = **2980** ± 68 N/m^2	μ (N/m^2)	------ ------	**2560** ± 140 (**2880** ± 514)	**3000** ± 110 ------	**3780** ± 220 ------
	μ_{approx}	------	2600	3700	4400
FE μ_{RH} = 1600 N/m^2	μ (N/m^2)	**1760** ± 270 (**1770** ± 90)	**1640** ± 70 (**1770** ± 190)	**1760** ± 90 ------	**1580** ± 70 ------
	μ_{approx}	1800	1700	1800	1600

TABLE 3

DYNAMIC SHEAR MODULUS ESTIMATES IN MOUSE BRAIN

		In vivo			*Post Mortem*		
		Anterior	**Middle**	**Posterior**	**Anterior**	**Middle**	**Posterior**
Cortical	Mean (N/m^2)	**14800**	**13800**	**12600**	**14600**	**14100**	**13900**
	± std. dev.	±2029	±1490	±1993	±49	±1287	±70
Sub-Cortical	Mean (N/m^2)	**18700**	**15300**	**16500**	**15400**	**14200**	**15400**
	± std. dev.	±2820	±1483	±3057	±2177	±802	±415